

# Experimental study on the high-damping properties of metallic lattice structures obtained from SLM

F. Scalzo<sup>a</sup>, G. Totis<sup>a,\*</sup>, E. Vaglio<sup>a</sup> and M. Sortino<sup>a</sup>

<sup>a</sup>Politechnic Department of Engineering and Architecture, Università di Udine, Via delle scienze 206, 33100 Udine, Italy

---

## ARTICLE INFO

### Keywords:

Additive Manufacturing  
Selective Laser Melting  
Lattice structure  
Damping  
Vibrations

## ABSTRACT

Modern additive manufacturing technologies allow the creation of parts characterized by complex geometries that cannot be created using conventional production techniques. Among them the Selective Laser Melting (SLM) technique is very promising. By using SLM it is possible to create lightweight lattice structures that may fill void regions or partially replace bulk regions of a given mechanical component. As a consequence, the overall mechanical properties of the final component can be greatly enhanced, such as the resistance to weight ratio and its damping capacity against undesired vibrations or acoustic noise. Nevertheless, only a few research works focused on the characterization of the dynamic behaviour of lattice structures, that were mainly investigated in the low frequency range or directly tested on some specific applications. In this work the dynamic behaviour of lattice structures in the medium-high frequency range was experimentally investigated and then modelled. For this purpose, different types of lattice structures made of AlSi10Mg and AISI 316L were measured. Experimental modal analysis was performed on the obtained specimens in order to assess the influence of lattice material and unit cell geometry on their global dynamic behaviour. Experimental results revealed that lattice structures have superior damping characteristics compared to solid materials having an equivalent static stiffness. Eventually, the classic Rayleigh model was found to be adequate - with some approximation - to explain the damping behaviour of a generic lattice structure.

---

## 1. Introduction

Additive Manufacturing Technologies (AMT) allow the production of 3D solid parts through layer-by-layer material addition. Modern AMT may overcome many of the typical constraints affecting the traditional subtractive technologies, thus offering new opportunities to industrial designers. Specifically, the most appealing advantages are: a greater design freedom, good or even higher mechanical performances, shorter lead time and effective production decentralization with respect to subtractive technologies. New revolutionary applications of AMT can be found in many strategic sectors such as aerospace, biomedical and dental, automotive and unmanned vehicles, energy and general mechanical industry [1].

From an engineering point of view, Selective Laser Melting (SLM) is among the most promising and effective AMT. It is a powder-bed technique using gas-atomized metal powders that are laid down layer-upon-layer and selectively melted by means of a focused laser beam. Fully dense metallic components can be 3D printed by SLM, whose properties are in some cases comparable to those obtained from forging [2].

By increasing the geometric complexity it is possible to considerably optimize the final performances of 3D printed parts obtained from SLM. For instance, the superior design freedom of SLM can be exploited by methods of topological optimization as it was recently shown in [3, 4, 5].

Alternatively, by working at the meso-scale some special porous or trabecular/lattice structures have been investigated in the last 5 years in order to obtain locally adjustable mechanical properties, as illustrated in [6, 7, 8, 9]. Lattice structures can be successfully applied for weight reduction [10, 11], for increasing the impact energy absorption [12, 13] and for heat exchange enhancement [14, 15]. However, only a few authors focused on the manufacturability limits of SLM that may hinder the realization of generic lattice structures [16, 17].

---

\*Corresponding author: giovanni.totis@uniud.it; Tel. +39 0432 558258  
ORCID(s):

**Table 1**

Summary of recent research works studying lattice structures' mechanical properties.  $\mu$ CT=micro-computed tomography; BCC=body centered cubic; BCCZ=body centered cubic with vertical struts; DIC=digital image correlation; ECC=Edge Centre Cube; EDS=energy dispersive spectrometer; FBCCZ=BCCZ with 45° struts across cube faces; FCC=face centered cubic; FCCZ=FCC with vertical struts; F2BCC=BCC with 45° struts across cube faces; FEA=finite element analysis; RD=rhombic dodecahedron; SEM=scanning electron microscopy; SHPB=Split Hopkinson Pressure Bar; VC=vertex cube.

Ref.	Date	Unit cell geometry			Cell topology	Material	Testing strategy	Experimental method
		Lattice size Nx x Ny x Nz	Cell size [mm]	Strut diameter [mm]				
[18]	2019	5x5x(1,3,5,7)	10	1	BCC, BCCZ	AlSi10Mg	Compression	SEM, $\mu$ CT, Uniaxial compression testing, FEA
[19]	2019	3x3x3	12	1,25	3D re-entrant lattices	AlSi10Mg	Compression	$\mu$ CT, Compression test, FEA
[20]	2019	4x4x4	5	wall thickness 0,3-0,5	gyroid structure	SS 316L	Compression	Optical microscope, $\mu$ CT, Compression test, SEM, CFD
[21]	2019	5x5x5	5	0,54-1	tetrakaidecahedron, diamond, BCC	SS 316L	Compression	Uniaxial compression and tensile tests, Confocal microscope, SEM, EDS, FEA
[17]	2018	10x10x15	2-4	0,3	BCC, BCCZ, FCC, FCCZ	Inconel 625	Compression	$\mu$ CT, Quasi-static uniaxial compression testing, FEA
[22]	2018	5x5x1,3,5,7	10	1	BCCZ	AlSi10Mg	Compression	Theoretical model, Uniaxial tensile tests, SEM, Quasi-static compression tests, FEA
[23]	2018	3x3x3	26,1	1,5	low-CTE lattice structure	Ti-6Al-4V	Compression	Compression test, FEA
[24]	2018	3x3x3	10	0,8-1,8	RD	SS 316L	Compression	Quasi-static compression test, FEA
[25]	2018	6x6x6	5	0,38-1,113	F2BCC	AlSi12	Compression	SEM, Uniaxial compression testing, FEA
[7]	2018	8x8x8	2	90% to 70% variable porosity	FCC, VC, ECC	SS 316L	Compression	$\mu$ CT, Uniaxial compression testing, FEA
[26]	2016	10x10x10	7,5	1	BCC, BCCZ, FCC, FCCZ, FBCCZ	AlSi12Mg	Compression	$\mu$ CT, Quasi-static uniaxial compression testing, FEA
[27]	2018	8x2x1	6,3	0,5-0,9	kagome	Ti6Al4V	Compression, three-point bending tests	Compression, Three-point bending tests, FEA
[28]	2019	6x6x18	4	0,6	DOD, BCC1, BCC2	AlSi10Mg	Tensile	SEM, Quasi-static tensile test, FEA
[29]	2017	4x4x18	4	0,3	rhombic dodecahedron, BCC1, BCC2	AlSi10Mg	Tensile	Uniaxial tensile tests, SEM, FEA
[30]	2018	5x5x14-5x5x5	2,8	0,75	f2ccz and hollow spherical	SS 316L	Tensile, compression, fatigue	Optical microscopy, SEM, EDS, DIC, Tension, compression, fatigue testing
[31]	2019	2x2x2	5	0,8	Dfcc, Dhex, FCC, BCC	Ti6Al4V	Impact	SHPB, FEA
[32]	2019	1x1x1	12x8	0,1-0,5	octet	Ti-6Al-4V	Impact	SHPB apparatus, High speed camera, SEM, FEA
[33]	2019	5x5x5-4x4x4	2-4	0,344-0,689	Octet truss, RD, Diamond, Dode-Medium	Inconel 718	Compression, impact	$\mu$ CT, Compression test, SHPB apparatus, FEA
[34]	2018	2x4x6	4	1	BCC	SS 316L	Force controlled cyclic loading (0,1,1,10 Hz)	SEM, Optical microscope, Universal testing machine, FEA
[35]	2020	RLC:2-8x2-8x1,5-7,5 RLV:2-8x2-8x1,5-7,5 IR:2-8x2-8x1,5-7,5	varies	RLC:2,08 RLV:2-3 IR:2-3	RLC, RLV, IR	AlSi10Mg	Vibration testing (shaker)	Evolutionary algorithm, Shaker, FEA
[36]	2018	2x2x2	25	1.5	BCC and variations	Nylon 12	compression, impact (vibrations)	Mathematical model, Universal tensile test machine, FEA

Recent research works studying lattice structures properties are summarized in Table 1. Most authors focused on the elasto-plastic behavior of lattice structures in quasi-static conditions (tension/compression) or subjected to dynamic impact or fatigue testing. On the contrary, only a few investigated their dynamic behavior in terms of damping properties. Up to authors' knowledge only Rosa et al. in [34] measured the damping capacity of lattice structures made of AISI 316L stainless steel under low frequency sinusoidal excitation (less or equal to 10Hz), demonstrating that lattice structures have a higher damping capability than bulk specimens. This behavior was associated to amplitude dependent internal friction phenomena, mainly occurring at beam joints and in longitudinal beams.

In order to evaluate the damping behavior of lattice structures at higher frequencies, the authors of this work recently performed experimental modal analysis on SLM lattice structures made of AlSi10Mg [37]. By so doing, the enhanced damping properties of some specific lattice geometries were proven when considering the small amplitude, free oscillations of the specimens at their resonance frequencies (about 700 Hz).

However, no further information about the dynamic behavior of lattice structures in the medium-high frequency range is available for other materials.

In this work, the damping properties of SLM manufactured lattice structures made of AISI 316L austenitic stainless steel were experimentally investigated and compared to the former results found with AlSi10Mg.

The work is based on two designs of experiments. In the first design, the influence of lattice material and of unit cell geometry (for a given multiple-cell macroscopic geometry) is studied by performing 3D printing and experimental modal analysis (section 2). In the second design, the influence of multiple-cell macroscopic geometry is investigated, and a classical Rayleigh model is proposed for explaining the observed damping behavior (section 3). In the final section the main conclusions are drawn.

## 2. Effects of material and unit-cell geometry on the global dynamic behavior

### 2.1. Lattice structure and specimen design

Here the influence of the lattice structure material and of the elementary cell geometry on its global dynamic behavior is presented. In detail, the elementary cell geometry was varied by varying the cell size and the fill ratio, that was defined as the ratio between the diameter of the small beams composing the cell and the cell size, according to the design of experiments described in the following.

In addition to the light AlSi10Mg that was preliminarily tested in [37], the radically different AISI 316L stainless steel was investigated here. The aim was to further stress the initial hypothesis, i.e. that lattice structures may provide a better damping behavior with respect to the same material in full density bulk form. The choice of this material was also done for extending the results that Rosa et al. [34] found at very low frequencies (below 10 Hz).

Specimens were designed with the aim of evaluating their dynamic bending behavior thorough the pulse testing technique. For this purpose, a beam geometry was assumed with a square cross section of  $21 \times 21$  mm and a total axial length of 130 mm. The beam was composed of three connected parts: a full density lower base of 30 mm axial length, a central part of 60 mm axial length that was entirely filled with the lattice structures and a full density upper base of 40 mm axial length. The number of cells along the axial (Z) direction was adapted for reaching the assumed length of 60 mm. During the measurements, the lower base was clamped on a vice while the upper base was hit by an impact hammer and inspected by an eddy current probe, as it will be illustrated in Figure 6.

The following specifications were considered:

- the final results should be comparable with those obtained in [37] with AlSi10Mg;
- elementary cell size and fill ratio should be in accordance with printability limitations and process-related constraints that were pointed out in literature, especially by Mazur et al.[16];
- all the specimens should have a similar bending (static) compliance when they are clamped in cantilever configuration;
- the first resonance frequency of each specimen should be lower than about 2000 Hz in order to assure a reliable measurement of their dynamic compliance by means of pulse testing technique;
- the multiple-cell lattice structure should have a square cross-section with an integer number of cells along each side.

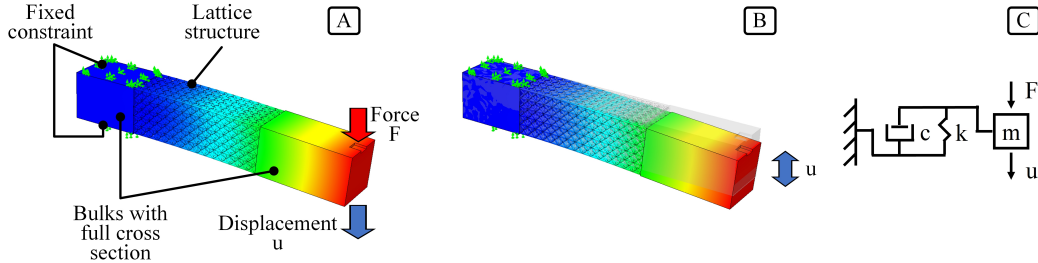


**Figure 1:** Physical and numerical modeling of specimens embedding the lattice structures: linear static FEA (A); modal FEA (B); equivalent model based on a single harmonic oscillator (C).

**Table 2**

Aluminum AISi10Mg and Stainless Steel AISI 316L material properties

Property	90° (horizontal)		45° (inclined)		0° (vertical)	
	AISi10Mg	AISI 316L	AISi10Mg	AISI 316L	AISi10Mg	AISI 316L
Yield Strength $R_{p,0.2}$ [N/mm]	211 ± 4	374 ± 5	215 ± 3	385 ± 6	205 ± 3	330 ± 8
Tensile Strength $R_m$ [N/mm <sup>2</sup> ]	329 ± 4	650 ± 4	346 ± 3	640 ± 3	344 ± 2	529 ± 2
Max. elongation $\Delta L/L$ [%]	9 ± 1%	≥ 15%	7 ± 1%	≥ 15%	6 ± 1%	≥ 15%
Young's Modulus $E$ [N/mm <sup>2</sup> ]	75 · 10 <sup>3</sup>	200 · 10 <sup>3</sup>	75 · 10 <sup>3</sup>	200 · 10 <sup>3</sup>	75 · 10 <sup>3</sup>	200 · 10 <sup>3</sup>

Accordingly, the FBCCZ elementary cell topology was assumed in order to optimize the stiffness-to-weight ratio by concurrently assuring SLM printability. Then, the sizing phase was carried out iteratively by performing linear structural FEA by means of SolidWorks Simulation module.

It is worth recalling that material properties of SLM-manufactured alloys may depend on the build direction and on the process parameters. Here the data provided by the powder manufacturer were used for the FEA material (reported in Table 2), since they were found in good accordance with other mechanical tests performed by the authors on 3D printed dog-bone specimens obtained under the same process conditions.

In order to simulate the clamping conditions of the vice, two opposite faces of the lower base were fixed with an ideal, perfect constraint. A unitary distributed load ( $F = 1$  N) was applied on a small surface located at the edge of the specimens upper base, and the corresponding average displacement  $u$  was obtained from the numerical calculations in order to derive the static compliance, as follows

$$G = \frac{1}{k} = \frac{u}{F} \left[ \frac{\mu\text{m}}{\text{N}} \right] \quad (1)$$






which is also the reciprocal of the static stiffness  $k$  [N/ $\mu\text{m}$ ], see Figure 1(A). Similarly, basic FE modal analysis was carried out in order to estimate the first natural frequency under the same clamping conditions, see Figure 1(B). In all cases, a mesh composed of tetrahedral elements was selected by performing a mesh convergence analysis. Mesh size refinement was automatically applied for small size features (e.g. the lattice struts) or where major stress variations were expected. At the end of the numerical, iterative phase the selected cell size levels were 2 and 4 mm, while the selected fill ratio levels were 0.200 and 0.275, see Table 3. The theoretical stiffness variation with respect to the reference specimen did not exceed  $\pm 15\%$  in all cases.

A full density square cross-section sample was also designed and taken as a reference for the final comparison (see Table 3 - sample E).

For the characterization of the global damping properties of the different specimens a model based on a single harmonic oscillator was assumed, as follows

$$W(j\omega) = \frac{1}{m(j\omega)^2 + c(j\omega) + k} = \frac{G}{\left(\frac{j\omega}{\omega_{n,1}}\right)^2 + 2\xi\left(\frac{j\omega}{\omega_{n,1}}\right) + 1} \quad (2)$$

**Table 3**  
First Design of Experiments

Name	A	B	C	D	E
Cell type	FBCCZ	FBCCZ	FBCCZ	FBCCZ	Full cross section
Cell size [mm]	4	4	2	2	12x12x60
Strut diameter [mm]	0.8	1.1	0.4	0.55	-
Fill ratio [ ]	0.200	0.275	0.2	0.275	-
Cells along X & Y	5	4	10	8	-
Cells number along Z	15	15	30	30	-
Total number of cells	375	240	3000	1920	-
Frontal view of lattice					

where  $m$ ,  $c$  and  $k$  are the modal mass, damping and stiffness coefficients respectively while  $G$  is the static compliance,  $\omega_{n,1}$  is the natural pulsation, and  $\xi$  is the damping ratio.

In order to normalize the measured damping with respect to the obtained static stiffness, a simplified Rayleigh model [38] was assumed, as follows:

$$c \cong \beta k \left[ \frac{Ns}{m} \right] \quad (3)$$

where the dependence on the modal mass that is typically present in the Rayleigh model was suppressed. Thus, the final comparison will be carried out in terms of the  $\beta$  coefficient that was determined as follows

$$\beta = \frac{c}{k} = c G = \frac{2\xi}{\omega_{n,1}} \quad [s] \quad (4)$$

## 2.2. Manufacturing through SLM

The CAD phase was carried out by using SolidWorks. Due to the fine details of the multiple-cell lattice structure, appropriate STL discretization parameters were selected in order to achieve an accurate STL model. Then, the STL models were further fixed, positioned and sliced by using Materialize Magics software.

A Concept Laser M2 Cusing was applied for the SLM production phase. The specimens were produced under an inert atmosphere of Argon to minimize oxidation phenomena. The inert gas inside the building chamber is extracted through a special vent. Accumulation of slag in the areas close to the vent is very likely, which may further cause inclusions and poor surface finish. Therefore, the specimens were placed on the opposite side of the platform with respect to the vent.

The samples were vertically aligned to exploit the self-supporting features of the FBCCZ topology and limit the residual stressed induced by the SLM process by minimizing the layers cross-sections. As a consequence, additional supports were only required under the lower base for an easy removal of the specimens by means of band-saw cutting.

In addition, they were oriented at  $45^\circ$  with respect to the coater blade, to obtain a progressive and uniform powder deposition.

Three replicates of each type of specimen made of AISI 316L were produced on three different building platforms, while only two replicates were produced when considering AlSi10Mg in the previous work [37]. Different random distributions of specimens were also adopted, in order to avoid systematic effects on the microstructure and on the mechanical properties. An example of specimens placement on the build platform is shown in Figure 2.

Chemical composition and particle-size distribution (PSD) of gas-atomized AlSi10Mg and AISI 316L powders are reported in Table 4. The adopted process parameters are listed in Table 5. The islands exposure strategy was selected in order to reduce thermal strains as much as possible. After the 3D printing process a stress relieving heat treatment was performed as prescribed by the powder manufacturer, as described in Table 6.

The first replicates of AlSi10Mg and AISI 316L specimens after separation from the build platform are visible in Figure 3.

**Table 4**

Chemical composition and particle-size distribution (PSD) of gas-atomized AlSi10Mg and AISI 316L powders

Material		Data		
AlSi10Mg	Chem. comp.	9.9%Si, 0.34%Mg, 0.12%O, 0.007%C, 0.006%Ti, balance Al		
	PSD	d10	d50	d90
		10.1 $\mu$ m	27.5 $\mu$ m	45.7 $\mu$ m
AISI 316L	Chem. comp.	17.7%Cr, 12.9%Ni, 2.39%Mo, 1.31%Mn, 0.66%Si, 0.016%C, balance Fe		
	PSD	d10	d50	d90
		19.8 $\mu$ m	29.9 $\mu$ m	45.1 $\mu$ m

**Table 5**

SLM process parameters

Material	Power [W]	Scan speed [mm/s]	Spot diam. [ $\mu$ m]	Layer thick. [ $\mu$ m]	Tracks overlap [%]
AlSi10Mg	200	650	120	25	30
AISI 316L	180	600	120	25	30

**Table 6**

Stress relieving annealing heat treatment

Material	Heat-up		Maintain		Cool-down	
	Time [h]	Temp [°C]	Time [h]	Temp [°C]	Time [h]	Temp [°C]
AlSi10Mg	1	240	6	240	q.s.	ambient
AISI 316L	3	550	6	550	q.s.	ambient

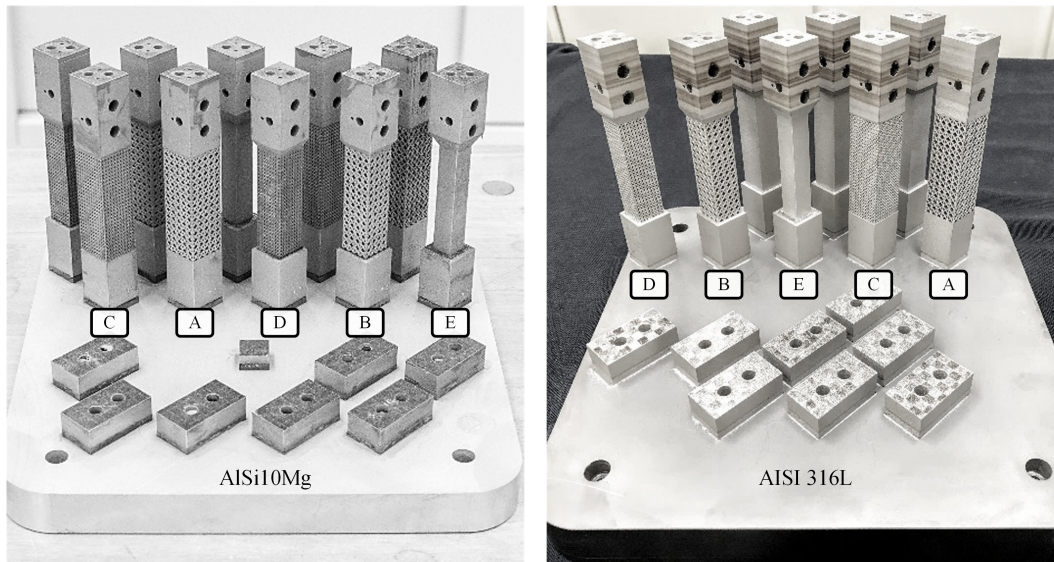


**Figure 2:** SLM-manufactured AlSi10Mg (left) and AISI 316L (right) specimens.

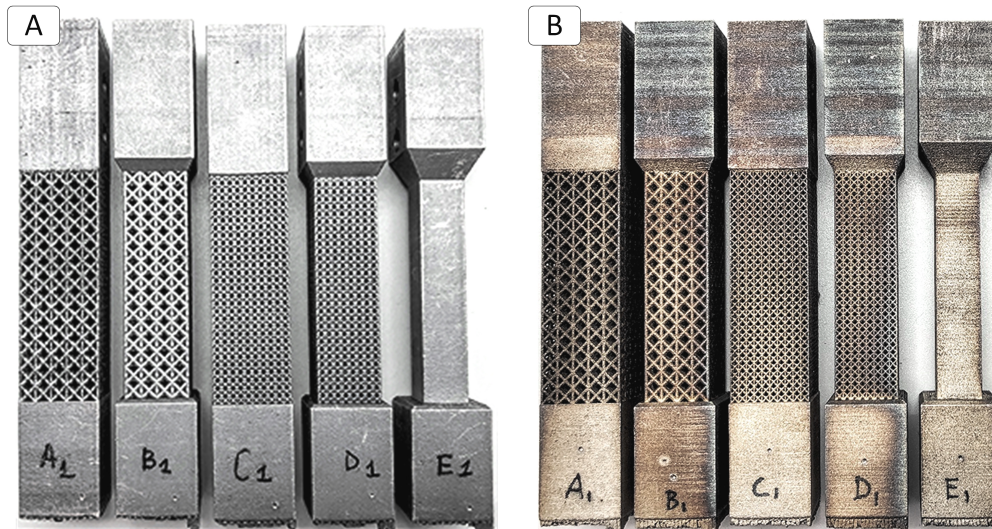


Figure 3: SLM-manufactured AlSi10Mg and AISI 316L specimens.

### 2.3. Lattice structure quality and dimensional accuracy

An optical digital microscope was used to inspect the quality of the lattice structures, that can be noticed in Figure 4. The dispersion due to process variability is clearly visible in the different replicates.

According to the dimensional measurements reported in Figure 5, struts diameters were larger than expected. The dimensional error was moderate for vertical struts, i.e. within  $\pm 0.15$  mm. On the contrary, it was considerably larger for inclined struts, that were particularly affected by the staircase effect and by the undesired adhesion of partially unmelted powders. These phenomena are responsible for a significant cell porosity reduction, that is particularly manifest for specimens type D that are characterized by a smaller cell size and by a larger fill ratio.

From the statistical analysis of dimensional errors (see boxplots illustrated in Figure 5), cell size and fill ratio have no significant effect on the dimensional error.

Only the lattice material has a direct and significant effect on dimensional accuracy: struts made of stainless steel were considerably larger than those made of aluminum alloy, probably because of a better choice of process parameters in the last case.

However no macroscopic deformations, cracks or failures were detected, thus confirming the satisfactory printability of vertically aligned FBCCZ lattice structures.

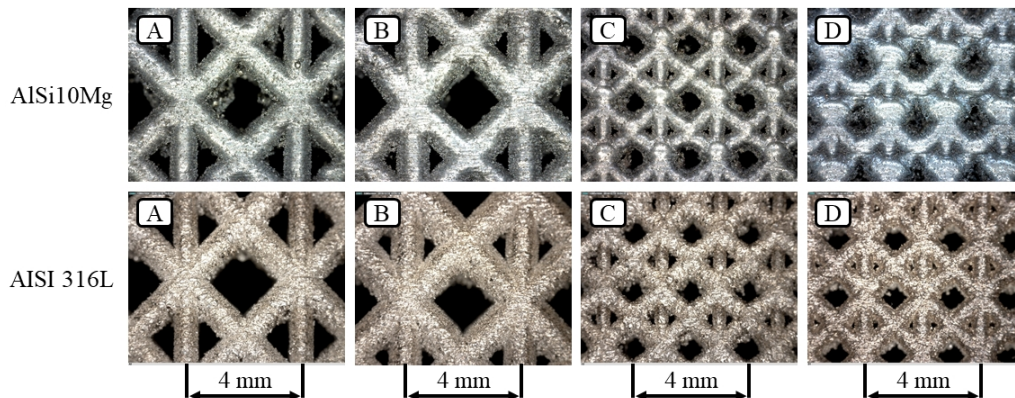
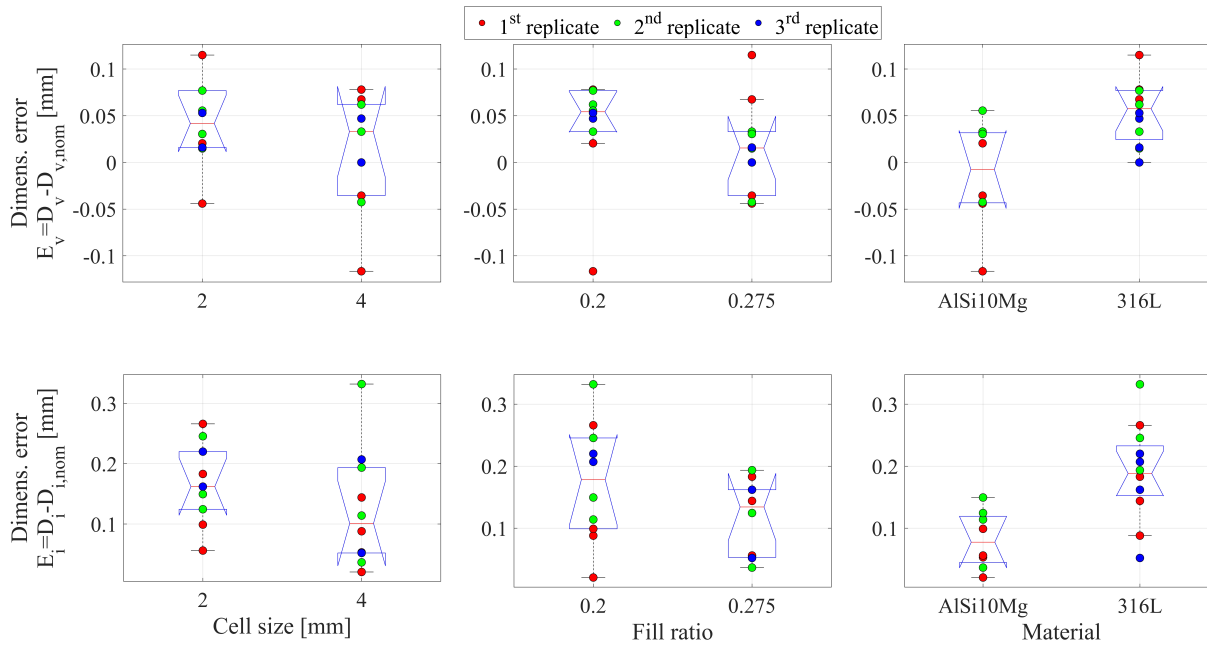


Figure 4: Detail views of the 3D printed lattice structures.



**Figure 5:** Dimensional errors affecting vertical and inclined beams/struts composing the produced lattice structures versus the design factors.

## 2.4. Dynamic identification

Experimental modal analysis was performed to identify the dynamic response of the specimens. For this purpose, each specimen was clamped by means of a vise on the rotary table of Haas VF-2TR CNC milling machine, see Figure 6 A.

The free tip of the specimen was hit by using an impact hammer Dytran type 5800B4 (sensitivity 2.41 mV/N), connected to a Kistler amplifier type 5134B. The resulting vibrations were measured by an eddy current probe Micro-Epsilon type ES1 (range about  $\pm 0.5$  mm) connected to an eddy NCDT3010-M controller. A triaxial accelerometer Kistler type 8763B (sensitivity 50 mV/g), positioned on the vice near the specimen, was also used to verify that the dynamic compliance of the vice was negligible in comparison to that of the specimen. Signal acquisition was carried out by a National Instruments cDAQ-9178 device with NI9215 modules, which was connected via USB to a PC. Sampling rate was set to 20 kHz. Data elaboration was executed in the MathWorks MATLAB environment.

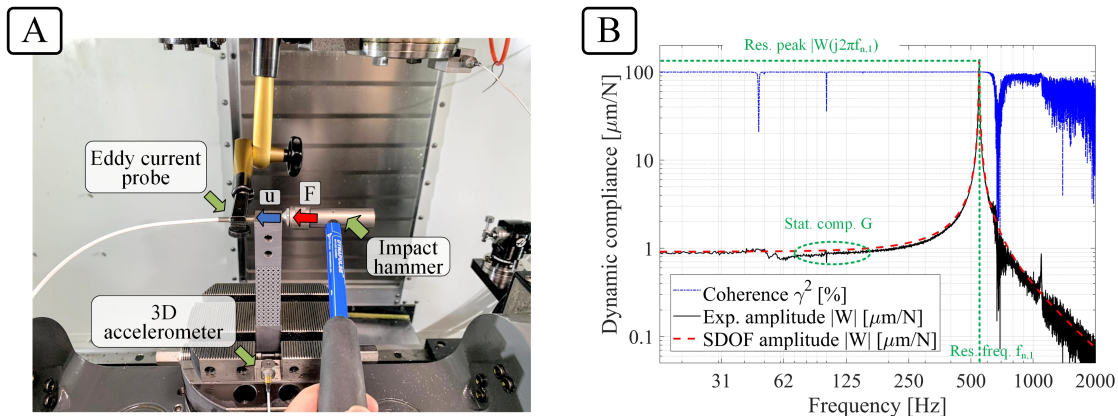


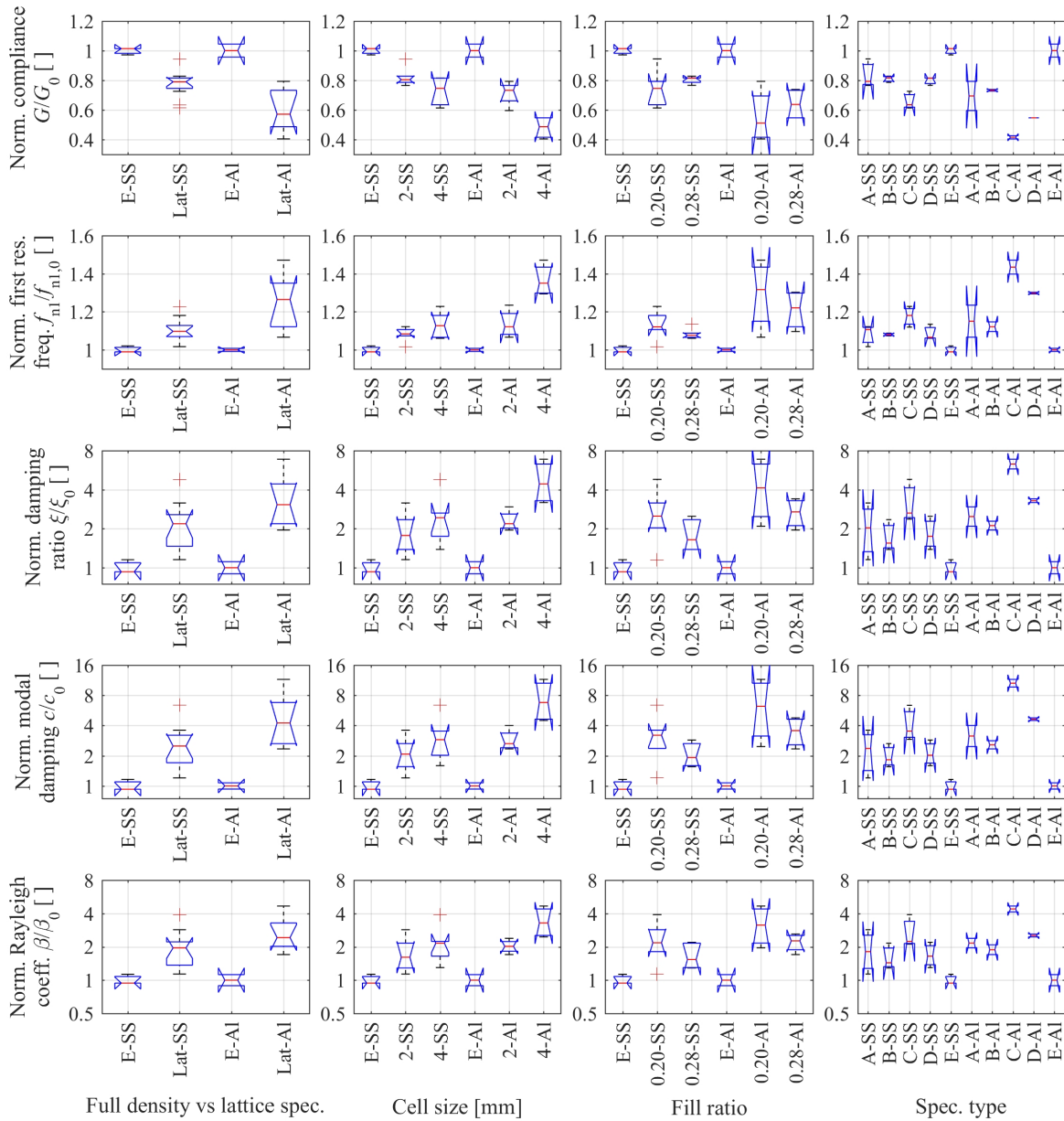
**Figure 6:** Identification of the global dynamic behavior of the lattice structures: experimental setup for pulse testing (A) and modal parameters extraction from the Empirical Transfer Function Estimate (B).



**Table 7**

Average values of modal parameters obtained from the full density reference specimens of type E.

Modal parameters	AISI10Mg(E)	AISI316L(E)
Avg. compliance [ $\mu\text{m}/\text{N}$ ]	1.83	0.97
Avg. first res. freq. [Hz]	588	539
Avg. damping ratio [ $10^{-3}$ ]	0.51	2.90
Avg. modal damping [Ns/m]	0.152	1.781
Avg. Rayleigh coeff. [ $\mu$ s]	0.277	1.72


**Figure 7:** Modal analysis results obtained on lattice specimens from the first experimental campaign.

The empirical transfer function estimate was then analyzed to extract the modal parameters of the dynamic model based on a single harmonic oscillator, see Figure 6(B). Specifically, static compliance was computed as the mean amplitude in the low frequency range 100÷150 Hz, as illustrated in Figure 6(B), while the other modal parameters were derived from the dominant resonance peak. In detail, the natural pulsation  $\omega_n$  was easily confused with the resonance pulsation  $\omega_r$ , while the damping ratio was estimated through the simple formula

$$\xi \cong \frac{G}{2|W(j\omega_r)|} \quad [] \quad (5)$$

which is valid for relatively small values of the damping ratio.

All the data obtained from modal analysis are illustrated in Figure 7. For each material the results of modal analysis were normalized by using the average values obtained from the full density reference specimens of type E reported in Table 7.

For both materials, the static compliances of the reference specimens (type E) are in good agreement with the preliminary FEM calculations. The specimens incorporating the lattice structures are on average 20% stiffer in case of stainless steel and 40% stiffer in case of aluminum as shown in the top of Figure 7. The reason is the larger strut diameters produced by the SLM process with respect to their nominal values, as proved in the previous subsection. As a consequence, the first resonance frequencies of lattice specimens are higher than expected.

Damping ratio  $\xi$ , modal damping  $c$  and Rayleigh coefficient  $\beta = c/k$  – all expressed in normalized and logarithmic form – are also compared in the same Figure.

For both materials, the specimens embedding the lattice structures have significantly higher damping properties with respect to the full density reference specimens. The main effect of cell size is significant only in the case of aluminum. The main effect of fill ratio is not significant neither for aluminum nor for stainless steel. In case of aluminum the combination of a small cell size with a small fill ratio (type C) is significantly higher than the other lattice types, as pointed out in [37]. This result is partially confirmed by lattice structures made of stainless steel, although the level of significance with respect to the other lattice types is lower in this case. In short, the type C lattice is the most recommended candidate for an effective damping of mechanical vibrations for both aluminum alloy and stainless steel.

### 3. Development and validation of a global Rayleigh damping model

#### 3.1. Lattice structure and specimen design

The experimental results of the first phase confirmed the enhanced damping properties of the lattice structures with respect to the full density reference specimens, even when considering the normalized  $\beta$  coefficient of the simplified Rayleigh model. On average, elementary cells having a minimum cell size of 2 mm proved to be more effective for attenuating mechanical vibrations.

Afterwards, a second design of experiments was carried out in order to assess the influence of the multiple-cell macroscopic geometry on the overall dynamic behavior.

FBCCZ unit cell topology was selected. Beams diameter and unit cell size were equivalent to those of A and C samples described before. By so doing it was possible to deepen the knowledge about the most promising type C lattice structure and to assess the influence of cell size on the global dynamic behavior, for a fixed fill ratio.

The same AISI 316L stainless steel of the first experimental campaign was chosen.

Specimens were designed with an upper base useful for the application of external loads and a lower base to ensure a solid grip with the vice. The size of the two bases was chosen in order to reduce printing time, while the central part of the beam-like specimen integrates the lattice structure. Also in this case the first natural frequency had to be lower than about 2500 Hz to allow a reliable modal analysis. Thus, factors levels were chosen by evaluating the results of FE simulations.

First of all, the diameters of the inclined beams composing each elementary cell were increased of 0.2 mm to take into account the systematic dimensional errors highlighted by the first experimental campaign.

It is important to notice that the most accurate numerical results can be obtained by discretizing the lattice structure with tetrahedral and hexahedral solid elements (Ansys SOLID186). This would require huge computational resources and a long elaboration time. In order to complete the design phase in a reasonable time, a first attempt was made by adopting a mixed mesh with ANSYS Mechanical. Specifically, circular cross-section Timoshenko beam elements

**Table 8**  
Second Design of Experiments.

Factors	Levels		
	-1	0	1
Length (X-axis) [mm]	12	20	28
Width (Y-axis) [mm]	12	20	28
Height (Z-axis) [mm]	48	60	72
Cell size [mm]	2	/	4

(BEAM189) were chosen for representing the lattice beams that were coupled at joints' centres. This considerably reduced the total number of nodes. Nevertheless, such solution was far less accurate than that obtained by only using solid elements, because simple Timoshenko beams having a uniform beam diameter do not correctly represent the joint regions. As a consequence, the static compliances as well as the first natural frequencies predicted by FEA were affected by a large estimation error of  $\pm 25\%$ .

In the last decade some effective strategies have been proposed for improving the computational efficiency of FE models of lattice structures [39, 40, 41]. Here an advanced mixed mesh strategy was applied, that was strongly based on the work of Guo et al. [41].

1. A sphere incorporating the joint region was determined from the geometric procedure proposed by such authors.
2. Each Timoshenko beam was split into three parts: a central part and two parts located at beam joints. The length of each joint beam element was set equal to the radius of the sphere determined before. After trial and error, the diameter of the joint beam elements was increased of +40% in order to better represent the effective joint stiffness. By so doing, lattice stiffness errors were compensated.
3. The mass density of the resulting lattice mesh composed of non-uniform Timoshenko beams was modified such that the total lattice mass was equal to the true value, that was already correct when adopting the solid mesh. Mass overestimation was due to the mass of the joint elements that are partially overlapped when approaching the joint center. By so doing, lattice natural frequency errors were compensated.

The main differences between solid mesh, simple mixed mesh and advanced mixed mesh can be seen in Figure 8.

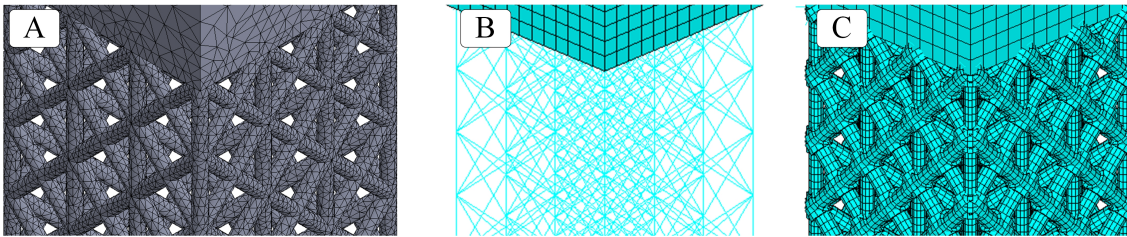


**Figure 8:** Detail view of tetrahedral mesh (A), Timoshenko beam mesh (B) and expanded view of the beam mesh highlighting joint diameter oversizing based on [41] (C).

Here the main factors of the design of experiments were the lattice cell size and the three sizes  $L_x$ ,  $L_y$  and  $L_z$  of the lattice parallelepiped of each specimen. The factor levels summarized in Table 8 were selected by considering the results of some preliminary numerical simulations. Thus, a  $2 \times 3 \times 3 \times 3 = 54$  full factorial design was planned. Cross-sections of the chosen lattice structures are illustrated in Figure 9. Lattice structures type A and C were included as central points of the design, that is therefore an extension of the former. However, only 36 different specimens needed to be actually produced, since half of them could be measured twice by simply changing their orientation in the  $XY$  plane.

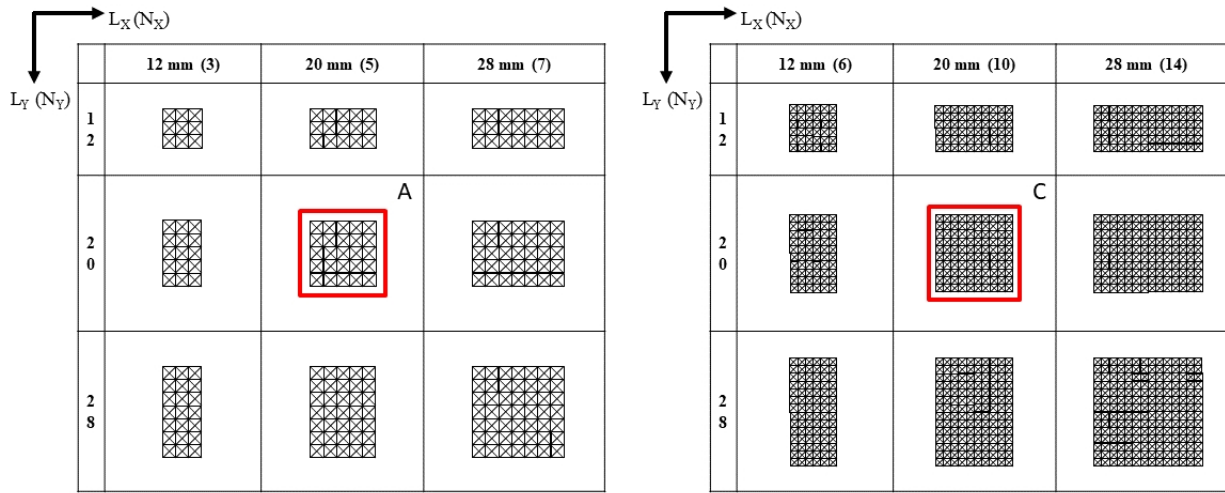


Figure 9: Cross-section views of the lattice specimens investigated during the second experimental campaign.

### 3.2. SLM manufacturing

Tools and equipment for preparing the print job were the same used for the production of the specimens of the first experimental campaign.

The 36 specimens were produced on three different platforms, by grouping them with respect to their total height, i.e. with respect to the  $L_z$  factor. By so doing, the same process conditions were maintained for all cross-sections of each lattice structure, in order to avoid any effect on the local mechanical properties that may depend on different thermal histories. As done before, specimens were randomly positioned on the platform and oriented at  $45^\circ$  with respect to the coater blade. On average each printing job required 6 days, for a total of 18 days. Then, all specimens were subjected to stress relieving heat treatment (see Table 6). The obtained specimens having  $L_z = 48$  mm,  $L_z = 60$  mm and  $L_z = 72$  mm are visible in Figure 10(A), (B) and (C) respectively.

The optical microscope confirmed the good quality and dimensional accuracy of the obtained parts, in accordance with the dimensional results presented in the previous section.

A set of reference, full density specimens were designed and produced a posteriori, i.e. after measuring the as-built lattice specimens, in order to further assess the superior damping properties of the lattice structures.

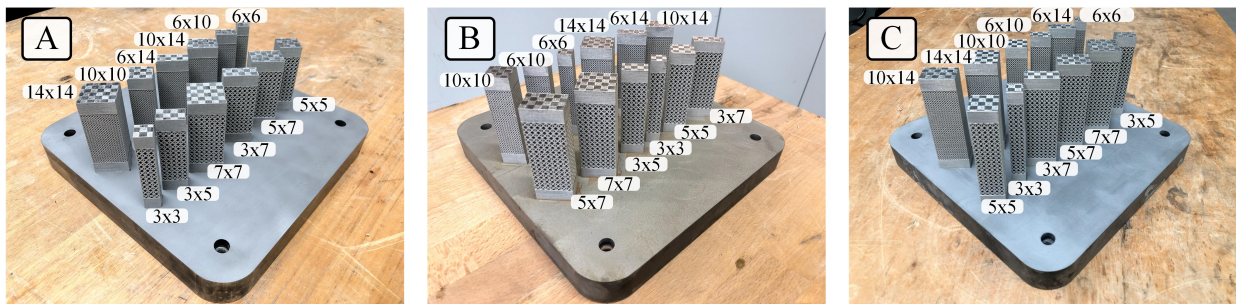


Figure 10: Specimens that were 3D printed for the second experimental campaign.

### 3.3. Dynamic characterization

Dynamic identification was accomplished by means of pulse testing by using the same experimental setup and procedures that were adopted for the first experimental campaign (Figure 6).

The results of experimental modal analysis confirmed that the bending behaviour of all the specimens in cantilever configuration was dominated by a single harmonic oscillator. Accordingly, the measured Empirical Transfer Function

Estimates (ETFEs) could be approximated by an equivalent single harmonic oscillator, that was univocally determined by its modal mass, stiffness and damping. Hence, all damping properties could be derived from measurements.

However, in the present case it was not possible to adopt the same simplified mass-spring-damper system for all the specimens, because their shape – hence their modal parameters – varied considerably within this second design.

In order to take into account the real geometry of each specimen and its dynamic interaction with the clamping fixture, a complex FE model was required. In detail, FE simulations were carried out by also taking into account the vice deformability. The advanced mixed mesh composed of Timoshenko non-uniform beams for representing the lattice structure and solid elements for all the rest was implemented, as illustrated in Figure 11. A special ANSYS APDL routine was also developed for launching the iterative steps and the repeated calculations automatically. By so doing, the model complexity and the total elaboration time were considerably reduced.

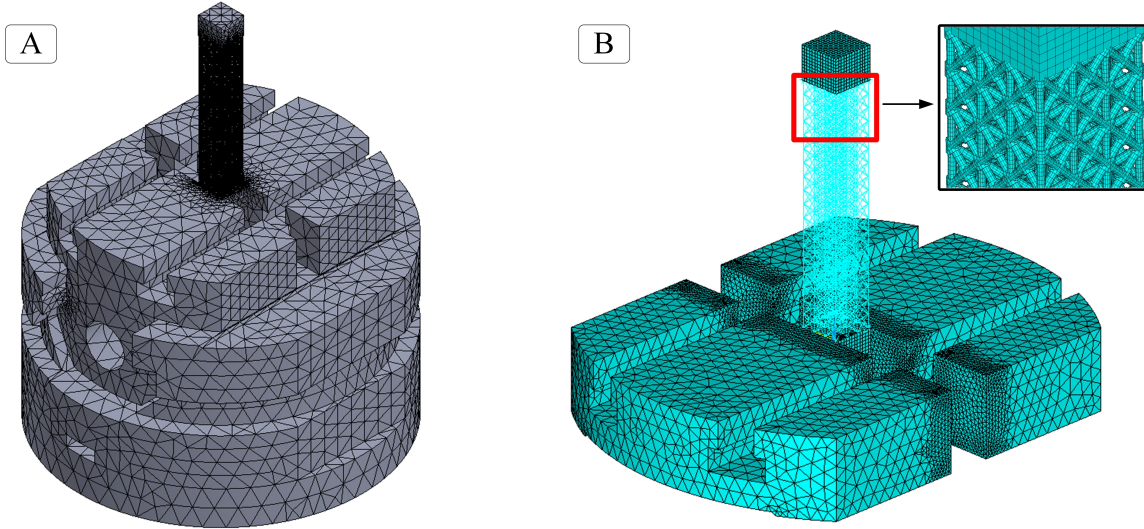


**Figure 11:** FE model of fixture-specimen assembly: tetrahedral mesh (A) compared to mixed mesh (tet-hex-beam) exploiting Timoshenko beam elements for specimen lattice section (B). Timoshenko beams with a larger diameter are adopted at beams connections, as illustrated in the enlarged view on the right.

Thus, the following general dynamic model was represented through the FE approach

$$\mathbf{M}\ddot{\mathbf{u}} + \mathbf{C}\dot{\mathbf{u}} + \mathbf{K}\mathbf{u} = \mathbf{F} \quad (6)$$

where  $\mathbf{M}$ ,  $\mathbf{C}$  and  $\mathbf{K}$  are the global mass, damping and stiffness matrixes,  $\mathbf{u}$  and  $\mathbf{F}$  are the generalized displacement and force vectors at nodes locations, respectively. Similarly to the one-dimensional approach adopted for the analysis of the first design, here the simplified Rayleigh damping model [38] was adopted through the approximation

$$\mathbf{C} \approx \beta \mathbf{K} \quad (7)$$

For a given  $\beta$  value ANSYS was applied to compute the resulting ETFE by simulating both the active force of the impact hammer and the corresponding vibration at the specimen free end. As expected, the obtained ETFE derived from FEA was dominated by a single harmonic oscillator. By a proper calibration of the  $\beta$  coefficient, it was possible to match the experimental and numerical values of the damping ratio corresponding to the dominant vibration mode. In short, from the comparison between the experimental and numerical ETFEs it was determined:

- the experimental static compliance  $G_{\text{exp}}$  at specimen free end and its numerical prediction  $G_{\text{FEM}}$  [ $\mu\text{m/N}$ ];
- the experimental first natural frequency  $f_{\text{n1,exp}}$  and its numerical prediction  $f_{\text{n1,FEM}}$  [Hz];
- the  $\beta$  coefficient of the Rayleigh model by requiring the equivalence between the measured and the predicted damping ratios, i.e.  $\xi_{\text{exp}} \cong \xi_{\text{FEM}}$ .

The relative errors between the numerical and experimental static compliances and natural frequencies were defined as follows

$$E_G = \frac{G_{\text{FEA}} - G_{\text{exp}}}{G_{\text{exp}}} [\%]; \quad E_{f_{n,1}} = \frac{f_{n,1,\text{FEA}} - f_{n,1,\text{exp}}}{f_{n,1,\text{exp}}} [\%] \quad (8)$$

In most cases the observed relative errors are smaller than  $\pm 15\%$ , see Figure 12. This satisfactory accuracy was achieved only by including the vice into the simulation. On the contrary, by assuming a perfectly rigid constraint at the specimen lower base the numerical predictions were much more inaccurate (relative error  $\pm 30\%$ ).

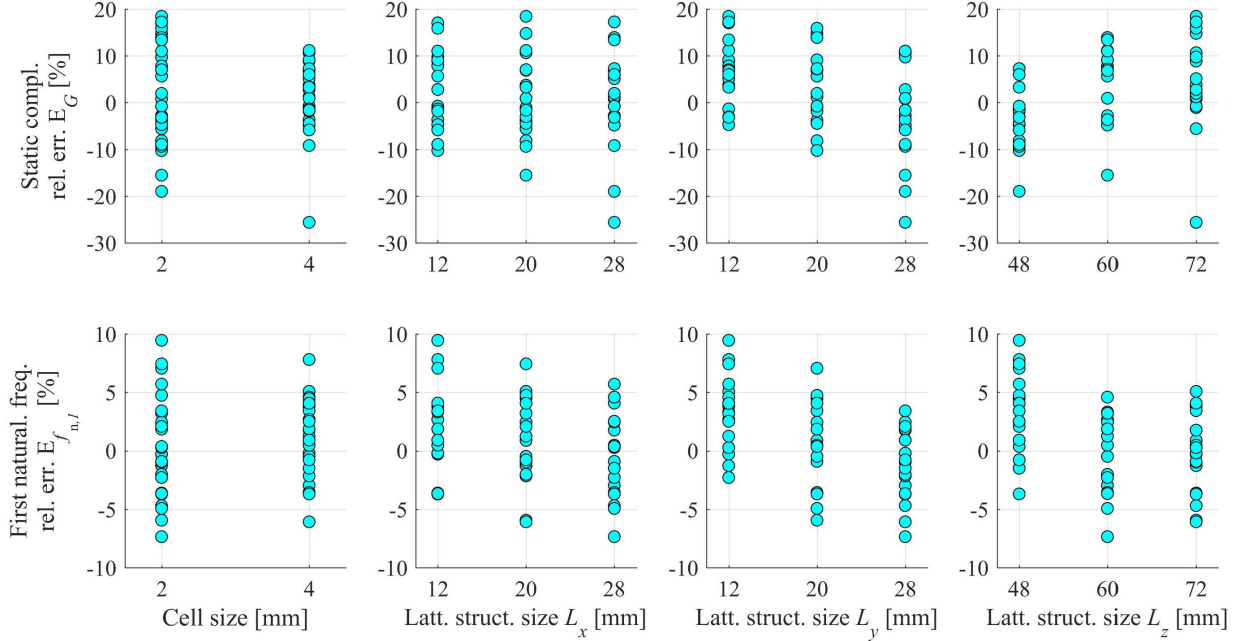


**Figure 12:** Relative errors between FEA numerical predictions and experimental values.

The main effects of the considered factors on the measured modal parameters can be observed in Figure 13. As expected, the static compliance and the first natural frequency depend on the considered factors, in good accordance with the FE model predictions.

Data analysis confirmed that lattice structures have significantly higher damping properties with respect to full density reference specimens.

All damping properties do not significantly depend on the size of the lattice elementary cell, thus rectifying the results obtained from the first campaign. However, they significantly vary when the sizes of the lattice region are varied. It is worth recalling that the variation of damping ratio  $\xi$  and modal damping  $c$  could be the consequence of modal mass and modal stiffness variations that were not constant among different specimens. On the contrary, the  $\beta$  coefficient should be scale-independent since it represents the scale-independent connection between damping and stiffness properties of the lattice region, as assumed in Equation 7.

An ideal Rayleigh model (without the mass-dependent term) would imply that the proportionality constant  $\beta$  was a scale independent constant. Since damping phenomena are generally stochastic, such constant may be approximated by a lognormally distributed random variable. Unfortunately here some additional scale-dependent trends of  $\beta$  are visible in Figure 13.

In order to better interpret such dependencies let us first notice that the order of magnitude of the  $\beta$  coefficient for the full density reference samples made of stainless steel was

$$\bar{\beta}_E \approx 1\mu s \quad (9)$$

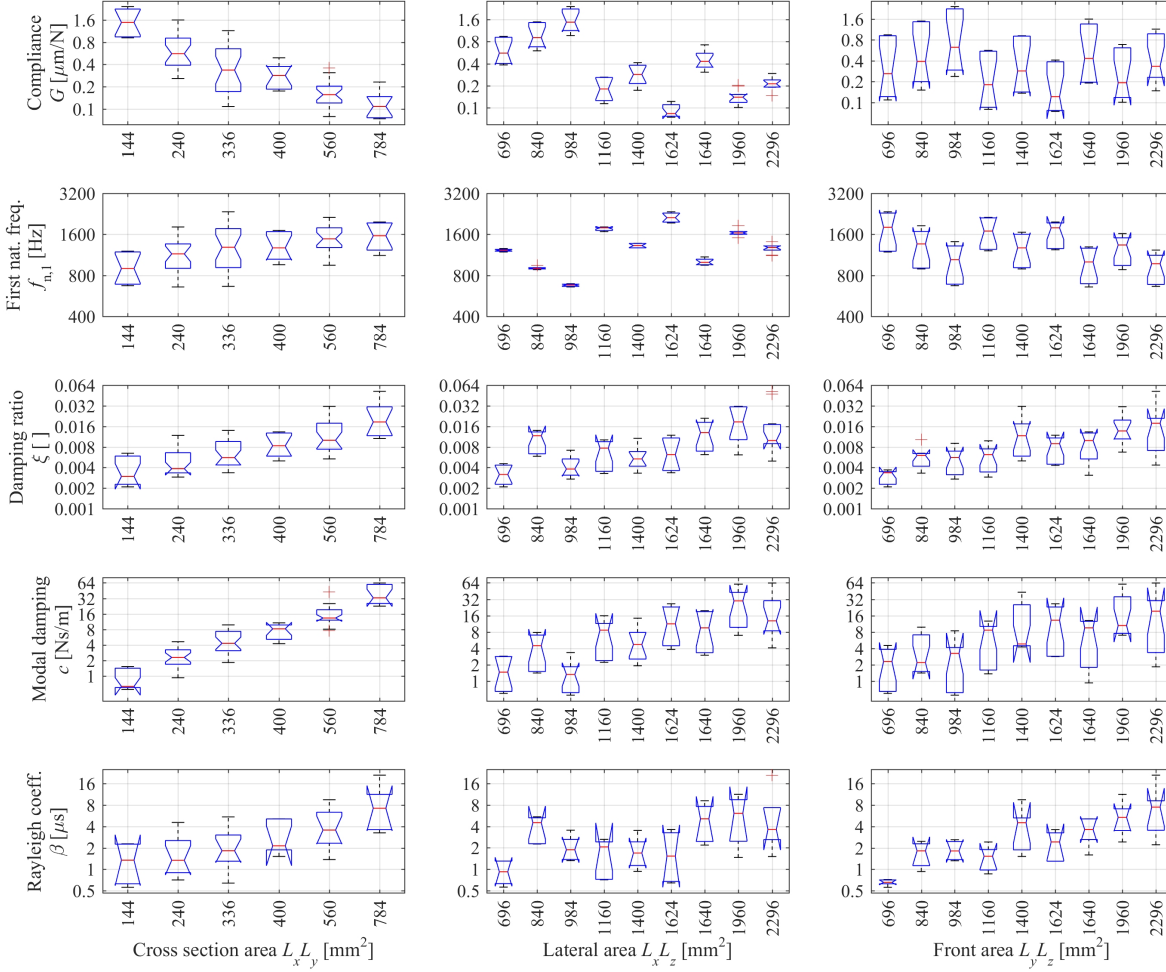


**Figure 13:** Modal analysis results obtained from the second experimental campaign.

as it was also confirmed by measuring the additional full density specimens that were 3D printed at the end of this second design.

Therefore, it is reasonable to normalize the  $\beta$  values obtained here by means of such quantity, by introducing

$$\beta' = \frac{\beta_{\text{exp}}}{\bar{\beta}_E} \quad (10)$$

The behavior of this coefficient can be expressed as follows

$$(\log \beta') \cong \underbrace{f_0(L_{x0}, L_{y0}, L_{z0})}_{\text{scale-indep. term}} + \underbrace{f_1(\Delta L_x, \Delta L_y, \Delta L_z)}_{\text{scale-dep. emp. correction}} + \underbrace{\varepsilon}_{\text{random term}} \quad (11)$$

where  $f_0$  is the mean value of  $\log \beta'$  with respect to the considered points,  $f_1$  describes a scale-dependent correction that was not already incorporated into Equation 7 while  $\varepsilon$  is a further (normally distributed) random term representing the true stochastic nature of  $\log \beta'$ .

In the current case the analysis of variance highlighted that  $(\log \beta')$  does significantly depend on  $L_x$ ,  $L_y$ ,  $L_z$  and on the two-way interactions  $(L_x, L_y)$ ,  $(L_x, L_z)$ . The following model was obtained by performing the stepwise linear

regression in the logarithmic scale

$$(\log \beta') \cong -0.92 - 4.34 \log L_x + 0.5 \log L_x \log L_y + 0.85 \log L_x \log L_z \quad (12)$$

where all the sizes  $L_x$ ,  $L_y$  and  $L_z$  are given in [mm]. This model can explain the variability of  $(\log \beta')$  around its average value with a squared linear correlation  $R^2 = 0.74$ .

Accordingly, the sum of squares of the observed values – without removing the average term – yields

$$SS_{\log \beta'} = \sum_{i=1}^N (\log \beta'_i)^2 \cong \underbrace{N f_0^2}_{53\%} + \underbrace{N \sigma_{f_1}^2}_{34\%} + \underbrace{N \sigma_\varepsilon^2}_{12\%} \quad (13)$$

where  $\sigma_{f_1}^2$  is the variance associated to the  $f_1$  term while  $\sigma_\varepsilon^2$  is the variance associated to the random term  $\varepsilon$ . This means that the constant, scale-independent term  $f_0$  may approximately explain the order of magnitude of  $\beta'$ . However, the scale-dependent correction  $f_1$  would be required to explain the variability of such coefficient around its average value.

The main conclusion is that damping can be well approximated by a simple Rayleigh model provided that a scale dependent correction is also included.

Possible reasons that may explain the need of a scale-dependent correction are the friction with the air, the unknown contact-clamping conditions between specimen and vice, the dynamic coupling with the vice and variations of local or global mechanical properties that are induced by the printing process (e.g. the aggregation of partially unmelted powder or the presence of defects is higher within larger specimens).

#### 4. Conclusions

Literature review highlighted the lack of exhaustive experimental studies evaluating the dynamic behavior SLM-manufactured lattice structures in the medium-high frequency range.

In the first experimental design, the damping properties of lattice structures made of AISI 316L stainless steel obtained from the SLM process were investigated and compared to those of AISi10Mg.

Printing accuracy was sufficient but lower than expected due to the undesired aggregation of partially unmelted powders, to the laser penetration through the previous layers and to the staircase effect that caused larger diameters of the inclined struts.

In a previous work the AISi10Mg lattice of type C (small cell size of 2 mm and small fill ratio equal to 0.2) was characterized by a significantly higher damping in comparison with the reference, full density bulk material having approximately the same static compliance ( $\beta/\beta_0 \approx 3$ ). In addition, type C lattice had a better performance than type A and B having a larger cell size (4 mm).

In this work the significantly higher damping properties of lattice structures with respect to full density specimens were also confirmed for AISI 316L (for type C:  $\beta/\beta_0 \approx 2$ ) but no significant differences with respect to the other lattice types were observed in terms of  $\beta$  - though on average type C was better than the other types.

Afterwards, the adequacy of a global, scale-independent Rayleigh model for describing the observed damping properties of the lattice structures was evaluated by means of a dedicated experimental design. With this aim many specimens having different sizes were produced and tested.

In order to calibrate this second design and to obtain the final results a special FE procedure was developed. The vice had to be included into the simulation in order to achieve a satisfactory accuracy (relative error within  $\pm 15\%$ ) in terms of static compliance and first natural frequency prediction. An advanced mixed mesh comprising Timoshenko beams with non-uniform diameters and solid finite elements was also necessary to drastically reduce the total elaboration time.

According to the obtained results, the damping behavior of the lattice structures can be approximately described by a simplified Rayleigh model based on single  $\beta$  coefficient. This should be expressed as the sum of a scale-independent constant term plus a scale-dependent correction and a random term. The first may explain the 54% of the observed behavior, the second the 34% and the third the residual 12%. The reasons for the need of a scale-dependent correction are still not clear and deserve clarification in future research works. However, the proposed Rayleigh approach may provide a first, approximated description of the observed lattice damping properties.



It would be of further interest to continue the research in this field in the perspective of developing new lattice structures with enhanced damping properties, that may be successfully exploited for advanced engineering applications.

## Acknowledgments

The Laboratory for Advanced Mechatronics - LAMA FVG - of the University of Udine is gratefully acknowledged for technical support. LAMA FVG is an international research center for product and process innovation where the three universities of Friuli Venezia Giulia (Italy) cooperate for promoting R&D activities at academic and industrial level.

## References

- [1] Syed A.M. Tofail, Elias P. Koumoulos, Amit Bandyopadhyay, Susmita Bose, Lisa O'Donoghue, and Costas Charitidis. Additive manufacturing: scientific and technological challenges, market uptake and opportunities, 2018.
- [2] Haniyeh Fayazfar, Mehrnaz Salarian, Allan Rogalsky, Dyuti Sarker, Paola Russo, Vlad Paserin, and Ehsan Toyserkani. A critical review of powder-based additive manufacturing of ferrous alloys: Process parameters, microstructure and mechanical properties. *Materials and Design*, 144:98–128, apr 2018.
- [3] Stefan Junk, Benjamin Klerch, and Ulrich Hochberg. Structural optimization in lightweight design for additive manufacturing. In *Procedia CIRP*, volume 84, pages 277–282. Elsevier B.V., jan 2019.
- [4] B. Rankouhi, K. M. Bertsch, G. Meric de Bellefon, M. Thevamaran, D. J. Thoma, and K. Suresh. Experimental validation and microstructure characterization of topology optimized, additively manufactured SS316L components. *Materials Science and Engineering A*, 776:139050, mar 2020.
- [5] Andrea Merulla, Andrea Gatto, Elena Bassoli, Sorin Ion Munteanu, Bogdan Gheorghiu, Mihai Alin Pop, Tibor Bedo, and Daniel Munteanu. Weight reduction by topology optimization of an engine subframe mount, designed for additive manufacturing production. In *Materials Today: Proceedings*, volume 19, pages 1014–1018. Elsevier BV, jan 2019.
- [6] Zhong hua Li, Yun fei Nie, Bin Liu, Ze zhou Kuai, Miao Zhao, and Fei Liu. Mechanical properties of AlSi10Mg lattice structures fabricated by selective laser melting. *Materials and Design*, 192:108709, jul 2020.
- [7] Zefeng Xiao, Yongqiang Yang, Ran Xiao, Yuchao Bai, Changhui Song, and Di Wang. Evaluation of topology-optimized lattice structures manufactured via selective laser melting. *Materials and Design*, 143:27–37, apr 2018.
- [8] Y. J. Liu, D. C. Ren, S. J. Li, H. Wang, L. C. Zhang, and T. B. Sercombe. Enhanced fatigue characteristics of a topology-optimized porous titanium structure produced by selective laser melting. *Additive Manufacturing*, 32:101060, mar 2020.
- [9] Yangli Xu, Dongyun Zhang, Songtao Hu, Runping Chen, Yilei Gu, Xiangsen Kong, Jiongming Tao, and Yijian Jiang. Mechanical properties tailoring of topology optimized and selective laser melting fabricated Ti6Al4V lattice structure. *Journal of the Mechanical Behavior of Biomedical Materials*, 99:225–239, nov 2019.
- [10] Dongseok Kang, Sanghu Park, Yong Son, Simo Yeon, Sang Hoon Kim, and Ilyong Kim. Multi-lattice inner structures for high-strength and light-weight in metal selective laser melting process. *Materials and Design*, 175:107786, aug 2019.
- [11] Guoying Dong, Yunlong Tang, Dawei Li, and Yaoyao Fiona Zhao. Design and optimization of solid lattice hybrid structures fabricated by additive manufacturing. *Additive Manufacturing*, 33:101116, may 2020.
- [12] Miao Zhao, David Z. Zhang, Fei Liu, Zhonghua Li, Zhibo Ma, and Zhihao Ren. Mechanical and energy absorption characteristics of additively manufactured functionally graded sheet lattice structures with minimal surfaces. *International Journal of Mechanical Sciences*, 167:105262, feb 2020.
- [13] Yuexin Du, Dongdong Gu, Lixia Xi, Donghua Dai, Tong Gao, Jihong Zhu, and Chenglong Ma. Laser additive manufacturing of bio-inspired lattice structure: Forming quality, microstructure and energy absorption behavior. *Materials Science and Engineering A*, 773:138857, jan 2020.
- [14] J. Y. Ho, K. C. Leong, and T. N. Wong. Additively-manufactured metallic porous lattice heat exchangers for air-side heat transfer enhancement. *International Journal of Heat and Mass Transfer*, 150:119262, apr 2020.
- [15] Akihiro Takezawa, Xiaopeng Zhang, Masaki Kato, and Mitsuru Kitamura. Method to optimize an additively-manufactured functionally-graded lattice structure for effective liquid cooling. *Additive Manufacturing*, 28:285–298, aug 2019.
- [16] M. Mazur, M. Leary, M. McMillan, S. Sun, D. Shidid, and Milan Brandt. Mechanical properties of Ti6Al4V and AlSi12Mg lattice structures manufactured by Selective Laser Melting (SLM). In *Laser Additive Manufacturing: Materials, Design, Technologies, and Applications*, pages 119–161. Woodhead Publishing, jan 2016.
- [17] Martin Leary, Maciej Mazur, Hugh Williams, Eric Yang, Ahmad Alghamdi, Bill Lozanovski, Xuezhe Zhang, Darpan Shidid, Lena Farahbod-Sternahl, Gerd Witt, Ingomar Kelbassa, Peter Choong, Ma Qian, and Milan Brandt. Inconel 625 lattice structures manufactured by selective laser melting (SLM): Mechanical properties, deformation and failure modes. *Materials and Design*, 157:179–199, nov 2018.
- [18] Hongshuai Lei, Chuanlei Li, Jinxin Meng, Hao Zhou, Yabo Liu, Xiaoyu Zhang, Panding Wang, and Daining Fang. Evaluation of compressive properties of SLM-fabricated multi-layer lattice structures by experimental test and  $\mu$ -CT-based finite element analysis. *Materials and Design*, 169, may 2019.
- [19] Luchao Geng, Wenwang Wu, Lijuan Sun, and Daining Fang. Damage characterizations and simulation of selective laser melting fabricated 3D re-entrant lattices based on in-situ CT testing and geometric reconstruction. *International Journal of Mechanical Sciences*, 157-158:231–242, jul 2019.

- [20] Shuai Ma, Qian Tang, Qixiang Feng, Jun Song, Xiaoxiao Han, and Fuyu Guo. Mechanical behaviours and mass transport properties of bone-mimicking scaffolds consisted of gyroid structures manufactured using selective laser melting. *Journal of the Mechanical Behavior of Biomedical Materials*, 93:158–169, may 2019.
- [21] Tianlin Zhong, K. He, Huaixue Li, and Lechang Yang. Mechanical properties of lightweight 316L stainless steel lattice structures fabricated by selective laser melting. *Materials and Design*, 181:108076, nov 2019.
- [22] Chuanlei Li, Hongshuai Lei, Yabo Liu, Xiaoyu Zhang, Jian Xiong, Hao Zhou, and Daining Fang. Crushing behavior of multi-layer metal lattice panel fabricated by selective laser melting. *International Journal of Mechanical Sciences*, 145:389–399, sep 2018.
- [23] C. Mercer, J. Lee, and D. S. Balint. An investigation of the mechanical behavior of three-dimensional low expansion lattice structures fabricated via laser printing. *Composite Structures*, 206:80–94, dec 2018.
- [24] Xiaofei Cao, Shengyu Duan, Jun Liang, Weibin Wen, and Daining Fang. Mechanical properties of an improved 3D-printed rhombic dodecahedron stainless steel lattice structure of variable cross section. *International Journal of Mechanical Sciences*, 145:53–63, sep 2018.
- [25] Dheyaa S.J. Al-Saedi, S. H. Masood, Muhammad Faizan-Ur-Rab, Amer Alomarah, and P. Ponnusamy. Mechanical properties and energy absorption capability of functionally graded F2BCC lattice fabricated by SLM. *Materials and Design*, 144:32–44, apr 2018.
- [26] Martin Leary, Maciej Mazur, Joe Elambasseril, Matthew McMillan, Thomas Chirent, Yingying Sun, Ma Qian, Mark Easton, and Milan Brandt. Selective laser melting (SLM) of AlSi12Mg lattice structures. *Materials and Design*, 98:344–357, may 2016.
- [27] Kai Wei, Qidong Yang, Bin Ling, Haiqiong Xie, Zhaoliang Qu, and Daining Fang. Mechanical responses of titanium 3D kagome lattice structure manufactured by selective laser melting. *Extreme Mechanics Letters*, 23:41–48, sep 2018.
- [28] Xiaoliang Geng, Yahui Lu, Chao Liu, Weinan Li, and Zhufeng Yue. Fracture characteristic analysis of cellular lattice structures under tensile load. *International Journal of Solids and Structures*, 163:170–177, may 2019.
- [29] Xiaoliang Geng, Liyang Ma, Chao Liu, Chen Zhao, and Zhu Feng Yue. A FEM study on mechanical behavior of cellular lattice materials based on combined elements. *Materials Science and Engineering A*, 712:188–198, jan 2018.
- [30] Patrick Köhnen, Christian Haase, Jan Bültmann, Stephan Ziegler, Johannes Henrich Schleifenbaum, and Wolfgang Bleck. Mechanical properties and deformation behavior of additively manufactured lattice structures of stainless steel. *Materials and Design*, 145:205–217, may 2018.
- [31] Nan Jin, Fuchi Wang, Yangwei Wang, Bowen Zhang, Huanwu Cheng, and Hongmei Zhang. Failure and energy absorption characteristics of four lattice structures under dynamic loading. *Materials and Design*, 169:107655, may 2019.
- [32] Sindhura Gangireddy, Mageshwari Komarasamy, Eric J. Faierson, and Rajiv S. Mishra. High strain rate mechanical behavior of Ti-6Al-4V octet lattice structures additively manufactured by selective laser melting (SLM). *Materials Science and Engineering A*, 745:231–239, feb 2019.
- [33] Kavan Hazeli, Behzad Bahrami Babamiri, Joseph Indeck, Andrew Minor, and Hesam Askari. Microstructure-topology relationship effects on the quasi-static and dynamic behavior of additively manufactured lattice structures. *Materials and Design*, 176:107826, aug 2019.
- [34] Francesco Rosa, Stefano Manzoni, and Riccardo Casati. Damping behavior of 316L lattice structures produced by Selective Laser Melting. *Materials and Design*, 160:1010–1018, dec 2018.
- [35] Simone Andresen, Annette Bäger, and Christian Hamm. Eigenfrequency maximisation by using irregular lattice structures. *Journal of Sound and Vibration*, 465:115027, jan 2020.
- [36] Wahyudin P. Syam, Wu Jianwei, Bo Zhao, Ian Maskery, Waiel Elmadih, and Richard Leach. Design and analysis of strut-based lattice structures for vibration isolation. *Precision Engineering*, 52:494–506, apr 2018.
- [37] M. Sortino, G. Totis, F. Scalzo, and E. Vaglio. Preliminary investigation of static and dynamic properties of SLM lattice structures for robotic applications. In *Mechanisms and Machine Science*, volume 66, pages 260–267. Springer Netherlands, aug 2019.
- [38] D.J.Ewins. Modal testing: theory, practice and application. *Research Studies Press LTD.*, Second Edition, 2000.
- [39] R. Gümruk and R. A.W. Mines. Compressive behaviour of stainless steel micro-lattice structures. *International Journal of Mechanical Sciences*, 68:125–139, mar 2013.
- [40] G. N. Labeas and M. M. Sunaric. Investigation on the static response and failure process of metallic open lattice cellular structures. *Strain*, 46(2):195–204, apr 2010.
- [41] Honghu Guo, Aikihiro Takezawa, Masanori Honda, Chikara Kawamura, and Mitsuru Kitamura. Finite element simulation of the compressive response of additively manufactured lattice structures with large diameters. *Computational Materials Science*, 175:109610, apr 2020.